$CsSnI_3$ Solar Cells via an Evaporation-Assisted Solution Method

*Pengchen Zhu, Chuanlu Chen, Shuai Gu, Renxing Lin, and Jia Zhu**

The environmental friendly tin-based perovskite is attracting a lot of attention as a lead-free alternative in photovoltaic field. However, the uncontrollable quick crystallization of tin-based perovskite in traditional solution methods makes it challenging to form smooth and pin-hole free films, resulting in severe surface recombination and current leakage problem. Evaporation method, known as an effective way to produce smooth films with high coverage, has been rarely investigated in tin-based perovskites. Here, we demonstrate an evaporation-assisted solution (EAS) method in $CsSnI_3$ system, combining thermal evaporation with solution method, to produce rather uniform, dense and pinhole free $CsSnI_3$ films. Solar cells fabricated by our EAS method show an average power conversion efficiency (PCE) of 1.93% and a best PCE of 2.23%.

Organic-inorganic lead halide perovskite solar cells have achieved dramatic development in the past few years, with a record efficiency exceeding 22%.[1] The toxicity of lead remains as an obstacle on the way towards large-scale applications.[2–6] Complete replacement of lead by low-toxic lead-free perovskite element is quite imperative.[7–11] Among all the lead-free perovskite candidates, tin-based perovskites are attracting tremendous attention in the photovoltaic (PV) field.[8,11] The most feasible analogies of lead-based perovskite materials are $MASnI_3$ and $FASnI_3$, which possess the highest reported efficiency among all tin-based perovskites.[12–14] However, the fragmentation of the organic component (MA^+, FA^+) in these materials brings the intrinsic instability.[15] It has been revealed that the substitution of organic component by inorganic element (Cs^+) can significantly improve the stability,[11,16–20] especially under the thermal condition. Therefore, $CsSnI_3$, an all-inorganic tin-based perovskite, is considered to be a promising candidate on account of the above considerations.[25–30]

While the conventional one-step solution method remains as the main fabrication method of $CsSnI_3$ solar cells so far, film growth appears a serious issue due to the rapid crystallization of tin-based perovskite,[8,13,21,22] which makes it difficult to produce pin-hole free and dense films in solution process, compared to the lead analogy. Thus, the optoelectronic devices based on $CsSnI_3$ typically suffer from the inevitable surface recombination and current leakage problems resulting from the crystallization issue mentioned above.

Thermal evaporation method, known as an effective way to produce smooth film with high coverage, has been systematically investigated in lead-based perovskites.[23,24] However, it has not been widely applied in the tin-based systems.[25,26] Here, we demonstrated an evaporation-assisted solution (EAS) method, combining thermal evaporation with solution method, to obtain rather uniform, full-coverage, dense and pinhole free $CsSnI_3$ films. Compared to the conventional one-step solution method, the high-quality film obtained from our method eliminates the direct contact of hole transporting material (HTM) and electron transporting material (ETM) and reduces the consequent recombination. In addition, this evaporation assisted solution process can enable convenient tuning of SnF_2 addition, which is critical for tin-based perovskite systems. An optimized solar cell based on $CsSnI_3$ with a power conversion efficiency (PCE) of 2.23% has been demonstrated.

Figure 1 shows the scheme of our evaporation-assisted solution method. SnI_2 with SnF_2 (considering the easy oxidation of Sn^{2+}) is firstly deposited on the substrate (typically on mesoporous TiO_2) by a spin-coating method. After annealing, the SnI_2 film is transferred into the vacuum chamber for the next CsI deposition. The deposition rate and thickness of CsI film can be precisely controlled in this evaporation process. The sample after evaporation is annealed at 150°C for 10 min to ensure the sufficient inter-diffusion of each component. During this annealing process, the film turns from yellowish to black (Figure S1 and S2, Supporting Information), indicating that CsI and SnI_2 are difficult to diffuse at room temperature and can only react with each other at elevated temperature. From the cross-section scanning electron microscope (SEM) images (Figure S4, Supporting Information), we can clearly see that two separate layers turned into one after annealing step. We also fabricated $CsSnI_3$ films by sequential vapor deposition of SnI_2 and CsI to prove our assumption. Before annealing, the film shows both SnI_2 and CsI peaks and very weak $CsSnI_3$ peaks. However, when annealing the films at 150 °C for 10 min, the final film shows corresponding peaks only matching with $CsSnI_3$, which indicates SnI_2 and CsI have diffused and reacted with each other during the annealing step (Figure S3, Supporting Information).

The thickness of evaporated CsI is found to be a key parameter for the fabrication of efficient $CsSnI_3$ solar cells. Deficient or

Dr. P. Zhu, Dr. C. Chen, Dr. S. Gu, Dr. R. Lin, Prof. J. Zhu
National Laboratory of Solid State Microstructures
College of Engineering and Applied Sciences
Collaborative Innovation Center of Advanced Microstructures
Nanjing University
Nanjing 210093, China
E-mail: jiazhu@nju.edu.cn

DOI: 10.1002/solr.201700224

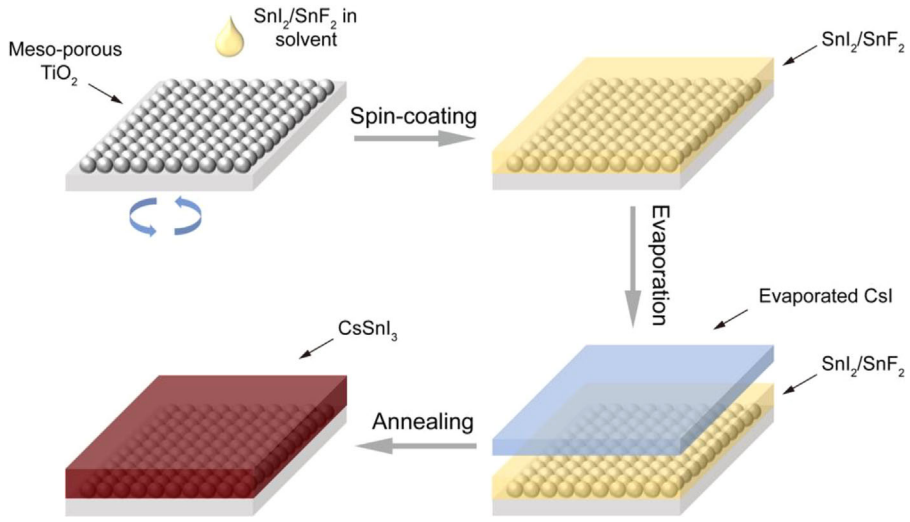

Figure 1. Schematic illustration of the evaporation-assisted solution method.

excessive evaporated CsI layer will result in the residue of SnI_2 or CsI, both of which have ill effects on the charge transport and the performance. We systematically adjusted the CsI thickness from 40 to 100 nm to carefully investigate the morphology, composition and device performance.

Firstly, we show the top-view SEM images of the SnI_2 film and $CsSnI_3$ films with different CsI thicknesses. **Figure 2**a shows the morphology of a typical solution-processed SnI_2 on meso-porous TiO_2 substrates. The formation of SnI_2 capping layer on TiO_2 is non-ideal and most of the SnI_2 is held in the pores of TiO_2 structure, because of the quick crystallization of SnI_2 during the annealing process, which is consistent with the previous study.[25] Figure 2b–f show the well-annealed $CsSnI_3$ films with different-thicknesses of CsI evaporated on SnI_2 substrates. When the CsI film is too thin (Figure 2b,c, corresponding to 40 and 52 nm CsI, respectively), there is not enough CsI to compensate SnI_2, leading to obvious pinholes. Increased CsI thickness will eliminate this problem and contribute to the formation of denser and bigger crystal grains (Figure 2d). However, when the thickness of CsI reaches 80 nm (Figure 2e), bright white impurities assigned to be CsI begin to emerge and the density of these impurities increases as the thickness of CsI further reaches 100 nm (Figure 2f). X-ray diffraction is also used to further confirm this effect. **Figure 3**a shows the XRD data of the $CsSnI_3$ films formed with different thicknesses of CsI. With 40 nm thick CsI, there exists a peak near 12.8° corresponding to SnI_2 indicating the SnI_2 residue. As the thickness of CsI increases to 80nm, a peak near 27.6° corresponding to CsI has arisen, a signal of excessive CsI. According to SEM images and XRD data above, it is clear that 66 nm CsI will be the optimized thickness with respect to the solution-process SnI_2 in our method. In addition, compared to the conventional solution method, these pin-hole free perovskite films from EAS method will bring about the

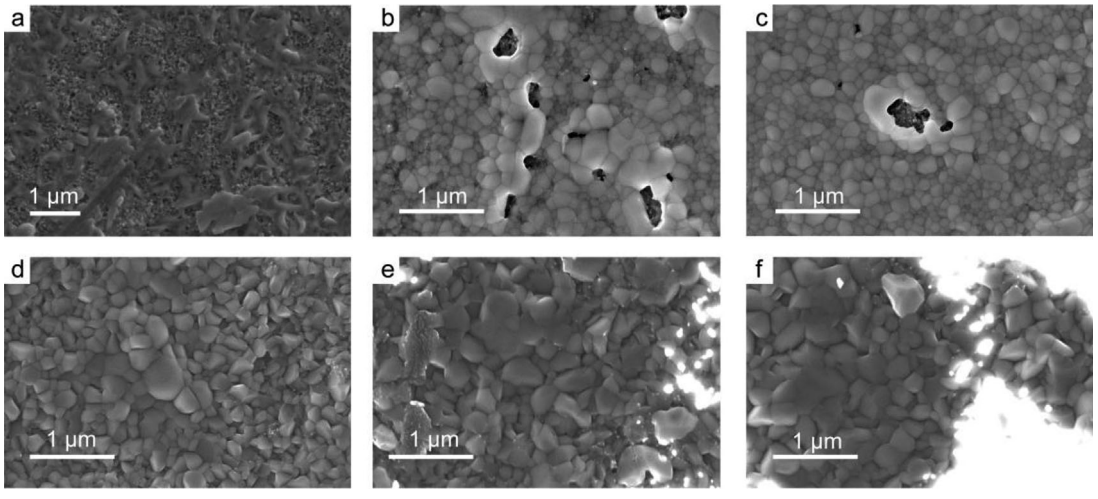

Figure 2. a) Top-view SEM images of solution-processed SnI_2 film on meso-porous TiO_2 after annealing. b)–f) Top-view SEM images of annealed $CsSnI_3$ films with different CsI thicknesses, b)–f) correspond to 40 nm, 52 nm, 66 nm, 80 nm, 100 nm thick CsI layers, respectively.

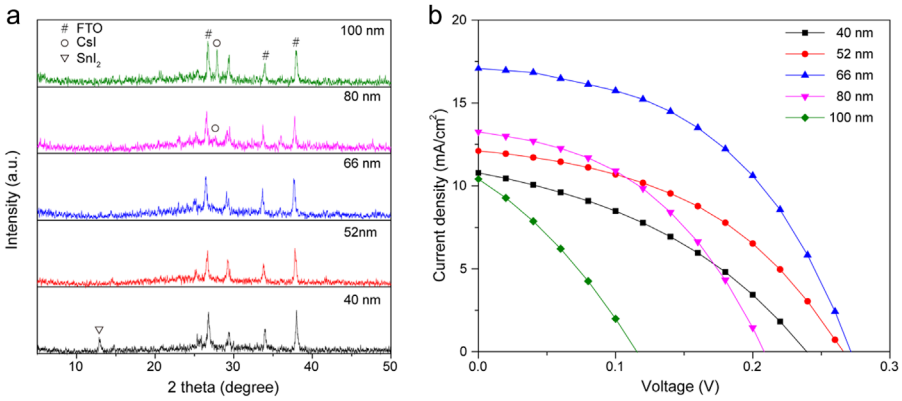

Figure 3. a) XRD patterns of $CsSnI_3$ films with different CsI thicknesses, 40 nm, 52 nm, 66 nm, 80 nm, 100 nm b) Typical *J–V* curves of $CsSnI_3$ based solar cells with different CsI thicknesses, 40 nm, 52 nm, 66 nm, 80 nm, 100 nm.

enhanced performance and stability (Figure S5–S8, Supporting Information).

We also fabricated solar cell devices employing a conventional meso-porous structure to investigate the performance. From bottom to top, the device consists of several layers of Fluorine-doped Tin Oxide (FTO), blocking TiO_2 (bl-TiO_2), mesoporous TiO_2 (mp-TiO_2), $CsSnI_3$ perovskite, spiro-MeOTAD and Au contact. The typical *J–V* curves of PV devices are clarified in Figure 3b. The optimized PCE of 2.20% is achieved in the device based on 66 nm CsI thickness. For the device fabricated with a thinner CsI film, the PCE values are 0.97%, 1.40% for CsI films of 40 nm, 52 nm, respectively. Compared to the optimized device, the decrease in V_{oc} and J_{sc} of thinner CsI results from the unreacted SnI_2 and pinholes, which hinder the charge transport and lead to current leakage. For devices with thicker CsI film of 80 and 100 nm, the PCE is 1.18% and 0.37%, respectively. As shown in Figure 2e,f, excessive white impurities on the surface impede the contact between the $CsSnI_3$ and HTM, which could also worsen the charge transport and thus have ill effects on short-circuit photocurrent.

In **Figure 4**a, we show the performance of our champion $CsSnI_3$ solar cell fabricated by the optimized recipe. This device

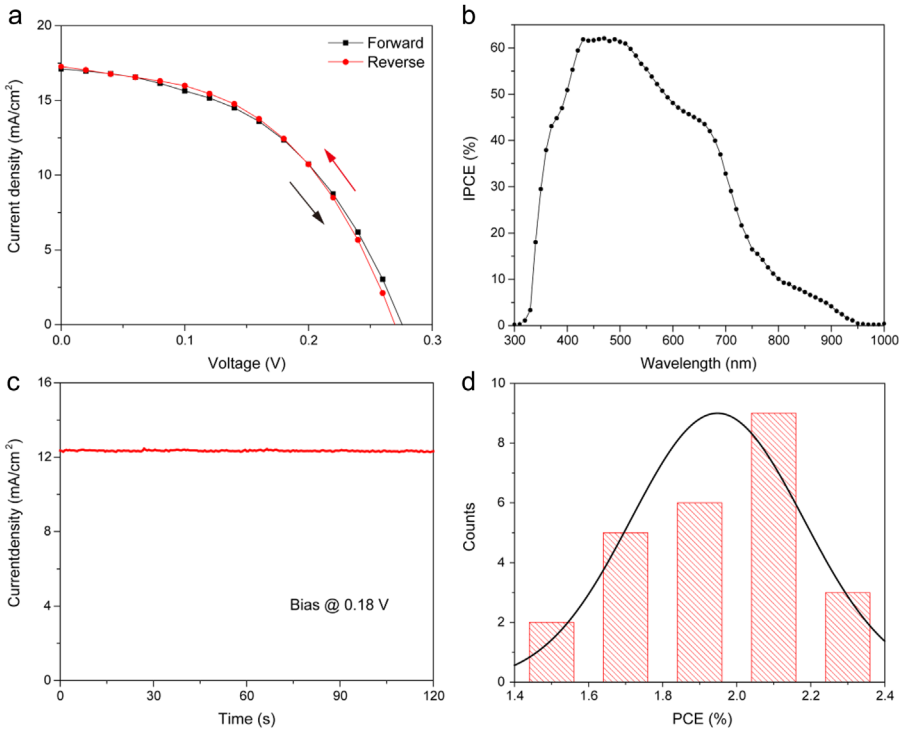

Figure 4. a) *J–V* curves of the champion device by EAS method in both forward and reverse directions. b) IPCE spectrum of the particular device (V_{oc} = 0.265 V, J_{sc} = 15.25 mA cm^{-2}, FF = 46.05% and PCE = 1.86%). c) Steady-state current density of champion device at a bias of 0.18 V. d) PCE histogram of 25 devices by EAS method.

demonstrates a PCE of 2.23% with an open-circuit voltage (V_{oc}) of 0.270 V, a short-circuit photocurrent density (J_{sc}) of 17.26 mA cm^{-2}, and a fill factor (FF) of 47.98% at reverse scan, and a PCE of 2.22% with a V_{oc} of 0.276 V, a J_{sc} of 17.10 mA cm^{-2}, and a FF of 47.15% at forward scan. The ignorable performance discrepancy at different scan directions illustrates that $CsSnI_3$ solar cell nearly obeys a hysteresis-free behavior. We further study the photoresponse of the particular solar cell ($V_{oc} = 0.265$V, $J_{sc} = 15.25$mA cm^{-2}, FF = 46.05% and PCE = 1.86%) by incident photon-to-electron conversion efficiency (IPCE) spectrum. The integrated current density is 12.05 mA cm^{-2}, slightly smaller than the short-circuit current density measured by *I–V* test (15.25 mA cm^{-2}). This result was also observed in $MASnI_3$-based perovskite solar cells in previous literature.[25] We attributed this mismatch to the unfilled trap states. Under one sun condition in the *I–V* test, the carrier density is sufficient to fill all the trap states, while it is insufficient under weak light intensity during the IPCE measurement. These traps will impede the transport of the photo-carriers, leading to a smaller integrated current. Figure 4c shows the photocurrent of our champion device at a constant bias of 0.18 V for 120 s, which is very steady at the value of 12.23 mA cm^{-2}, indicating the stability of $CsSnI_3$ solar cells under constant illumination. Based on the optimized recipe, we fabricated 25 devices in different batches to verify the reproducibility of our solar cells. The PCE histogram is shown in Figure 4d, exhibiting an averaged PCE of 1.93%. Further improvement in PCE can be expected for example with more suitable HTM/ETM materials.

In summary, we developed an evaporation-assisted solution (EAS) method, by which we can conveniently fabricate the pin-hole free tin-based perovskite films with adjustable addition of SnF_2. $CsSnI_3$ solar cells employing our method eliminate the direct contact between ETL and HTL and demonstrate the efficiency to 2.23%. It is expected that this method can be applied to various other kinds of perovskite films for optoelectronic applications.

Experimental Section

Materials: Anhydrous N,N-dimethylformamide (DMF, 99.8%), anhydrous dimethylsulfoxideand (DMSO 99.9%) were purchased from J&K. SnI_2 (99.99%) and tetrabutyl titanate and lithium bis (trifl uoromethanesulfonyl) imide were purchased from alfa aesar. SnF_2 (99%) was purchased from Aladdin. TiO_2 paste was purchased from dyesol. SnI_2 (containing SnF_2) solution was prepared by dissolving 1.0 mmol of SnI_2 (373 mg) and 30% SnF_2 (47.1 mg) were added into the mixture of 2mL of DMSO and DMF. The volume ratio of DMSO and DMF is 1:2.

Device Fabrication: FTO glasses were cleaned in acetone, ethanol and deionized water in an ultrasonic bath for 30 min respectively. After being drying with a nitrogen gun, the FTO substrates were treated in a UV ozone (UVO) cleaner for 30 min. A 50 nm TiO_2 blocking layer (bl-TiO_2) was deposited on the FTO substrates by spin coating the tetrabutyl titanate/ethanol solution, and then the substrates were annealed at 500 °C for an hour. After cooling to room temperature, the substrates were treated in UV-ozone for 20 min. Mesoporous TiO_2 (mp-TiO_2) layer was then deposited on the bl-TiO_2 by spin-coating the TiO_2 colloidal solution containing 1 g of TiO_2 paste diluted in 5 g of anhydrous ethanol solution at 4000 rpm for 30 s.Then the substrate was annealed at 500 °C for 30 min and treated in UV-ozone for 20 min after cooling to room temperature. The substrate was then transferred into glovebox. For SnI_2 deposition, the as-prepared SnI_2 solution was spin-coated on the mp-TiO_2 layer at 3000 rpm for 30 s. Then the film was annealed at 50 °C for 5 min and 100 °C for 10 min. Then the SnI_2 layer was transferred into the vacuum chamber for the CsI deposition. The thickness of CsI was detected by a sensor. Proper amount of CsI was evaporated thermally onto the SnI_2 layer and annealed at 150 °C for 10 min. Spiro-MeOTAD solution consisting of 72.3 mg spiro-MeOTAD, 28.8 μL of 4-tert-butyl pyridine and 17.5 μL of lithium bis (trifl uoromethanesulfonyl) imide (Li-TFSI) solution(520 mg Li-TSFI in 1 mL of acetonitrile) in 1ml of chlorobenzene, was spin-casted on the perovskite layer at 4000 rpm for 30 s. For counter electrode, Au was thermally evaporated at evaporation rate of 0.2 Å s^{-1}, reaching a thickness of 80nm. All the fabrication process was performed in the glove box filled with nitrogen. The water level is below 0.1 ppm and the oxygen level is below 10 ppm.

Optoelectronic Characterizations: The *J–V* characteristics of the devices were measured by a solar simulator (Enli Technology Co., Ltd SS-F5-3A) equipped with a Keithley 2400 digital source meter. The NREL-calibrated solar (Enli Technology Co., LtdSRC2020) was used to adjust the light intensity into one sun illumination (100 mW cm^{-2}). All the *J–V* tests were performed in the glovebox filled with nitrogen. The IPCE spectrum of perovskite films was measured with a monochromator (Newport 74125) and a power meter (Newport 2936-C). The devices were encapsulated by polymer and measured in air for the IPCE test.

Structure and Morphology Characterizations: The XRD images were characterized on a Rigaku Ultima X-ray IV diffractometer using a Cu Kα 3 deg min^{-1}. The SEM images were taken by a focused ion beam microscope (Dual-beam FIB 235, FEI Strata).

Supporting Information

Supporting Information is available from the Wiley Online Library or from the author.

Acknowledgements

We acknowledge the micro-fabrication center of National Laboratory of Solid State Microstructures (NLSSM) for technique support. This work is jointly supported by the State Key Program for Basic Research of China (No. 2015CB659300), National Natural Science Foundation of China (Nos. 11621091, 11574143), Natural Science Foundation of Jiangsu Province (Nos. BK20150056), the Project Funded by the Priority Academic Program Development of Jiangsu Higher Education Institutions (PAPD) and the Fundamental Research Funds for the Central Universities.

Conflict of Interest

The authors declare no conflict of interest.

Keywords

evaporation, inorganic, lead free, perovskite solar cells, tin

Received: December 6, 2017
Revised: January 27, 2018
Published online:

[1] W. S. Yang, B. W. Park, E. H. Jung, N. J. Jeon, Y. C. Kim, D. U. Lee, S. S. Shin, J. Seo, E. K. Kim, J. H. Noh, S. I. Seok, *Science* **2017**, *356*, 1376.
[2] A. Babayigit, A. Ethirajan, M. Muller, B. Conings, *Nat. Mater.* **2016**, *15*, 247.
[3] D. P. McMeekin, G. Sadoughi, W. Rehman, G. E. Eperon, M. Saliba, M. T. Horantner, A. Haghighirad, N. Sakai, L. Korte, B. Rech, M. B. Johnston, L. M. Herz, H. J. Snaith, *Science* **2016**, *351*, 151.
[4] N. J. Jeon, J. H. Noh, Y. C. Kim, W. S. Yang, S. Ryu, S. I. Seok, *Nat. Mater.* **2014**, *13*, 897.
[5] H. Zhou, Q. Chen, G. Li, S. Luo, T. B. Song, H. S. Duan, Z. Hong, J. You, Y. Liu, Y. Yang, *Science* **2014**, *345*, 542.
[6] P. Zhu, S. Gu, X. Shen, N. Xu, Y. Tan, S. Zhuang, Y. Deng, Z. Lu, Z. Wang, J. Zhu, *Nano Lett.* **2016**, *16*, 871.
[7] D. Cortecchia, H. A. Dewi, J. Yin, A. Bruno, S. Chen, T. Baikie, P. P. Boix, M. Gratzel, S. Mhaisalkar, C. Soci, N. Mathews, *Inorg. Chem.* **2016**, *55*, 1044.
[8] F. Hao, C. C. Stoumpos, D. H. Cao, R. P. H. Chang, M. G. Kanatzidis, *Nat. Photonics* **2014**, *8*, 489.
[9] W. Liao, D. Zhao, Y. Yu, C. R. Grice, C. Wang, A. J. Cimaroli, P. Schulz, W. Meng, K. Zhu, R. G. Xiong, Y. Yan, *Adv. Mater* **2016**, *28*, 9333.
[10] T.-B. Song, T. Yokoyama, S. Aramaki, M. G. Kanatzidis, *ACS Energy Lett.* **2017**, *2*, 897.
[11] D. Zhao, Y. Yu, C. Wang, W. Liao, N. Shrestha, C. R. Grice, A. J. Cimaroli, L. Guan, R. J. Ellingson, K. Zhu, X. Zhao, R.-G. Xiong, Y. Yan, *Nat. Energy* **2017**, *2*, 17018.
[12] W. J. Ke, C. C. Stoumpos, M. H. Zhu, L. L. Mao, I. Spanopoulos, J. Liu, O. Y. Kontsevoi, M. Chen, D. Sarma, Y. B. Zhang, M. R. Wasielewski, M. G. Kanatzidis, *Sci. Adv.* **2017**, *3*, e1701293.
[13] F. Hao, C. C. Stoumpos, P. Guo, N. Zhou, T. J. Marks, R. P. Chang, M. G. Kanatzidis, *J. Am. Chem. Soc.* **2015**, *137*, 11445.
[14] S. Shao, J. Liu, G. Portale, H.-H. Fang, G. R. Blake, G. H. ten Brink, L. J. A. Koster, M. A. Loi, *Adv. Energy Mater.* **2017**, 1702019.
[15] T. Leijtens, G. E. Eperon, N. K. Noel, S. N. Habisreutinger, A. Petrozza, H. J. Snaith, *Adv. Energy Mater.* **2015**, *5*, 1500963.
[16] R. J. Sutton, G. E. Eperon, L. Miranda, E. S. Parrott, B. A. Kamino, J. B. Patel, M. T. Hörantner, M. B. Johnston, A. A. Haghighirad, D. T. Moore, H. J. Snaith, *Adv. Energy Mater.* **2016**, *6*, 1502458.
[17] N. Wang, Y. Zhou, M.-G. Ju, H. F. Garces, T. Ding, S. Pang, X. C. Zeng, N. P. Padture, X. W. Sun, *Adv. Energy Mater.* **2016**, *6*, 1601130.
[18] W. Z. Li, J. W. Li, J. L. Li, J. D. Fan, Y. H. Mai, L. D. Wang, *J. Mater. Chem. A* **2016**, *4*, 17104.
[19] K. P. Marshall, M. Walker, R. I. Walton, R. A. Hatton, *Nat. Energy* **2016**, *1*, 16178.
[20] J.-W. Lee, D.-H. Kim, H.-S. Kim, S.-W. Seo, S. M. Cho, N.-G. Park, *Adv. Energy Mater.* **2015**, *5*, 1501310.
[21] M. H. Kumar, S. Dharani, W. L. Leong, P. P. Boix, R. R. Prabhakar, T. Baikie, C. Shi, H. Ding, R. Ramesh, M. Asta, M. Graetzel, S. G. Mhaisalkar, N. Mathews, *Adv. Mater* **2014**, *26*, 7122.
[22] S. J. Lee, S. S. Shin, Y. C. Kim, D. Kim, T. K. Ahn, J. H. Noh, J. Seo, S. I. Seok, *J. Am. Chem. Soc.* **2016**, *138*, 3974.
[23] M. Liu, M. B. Johnston, H. J. Snaith, *Nature* **2013**, *501*, 395.
[24] Q. Chen, H. Zhou, Z. Hong, S. Luo, H. S. Duan, H. H. Wang, Y. Liu, G. Li, Y. Yang, *J. Am. Chem. Soc.* **2014**, *136*, 622.
[25] T. Yokoyama, D. H. Cao, C. C. Stoumpos, T. B. Song, Y. Sato, S. Aramaki, M. G. Kanatzidis, *J. Phys. Chem. Lett.* **2016**, *7*, 776.
[26] D. Moghe, L. Wang, C. J. Traverse, A. Redoute, M. Sponseller, P. R. Brown, V. Bulović, R. R. Lunt, *Nano Energy* **2016**, *28*, 469.
[27] B. Wu, Y. Zhou, G. Xing, Qi. Xu, H. F. Garces, A. Solanki, T. W. Goh, N. P. Padture, T. C. Sum, *Adv. Fun. Mater.* **2017**, *27*, 1604818.
[28] L. Huang, W. R. Lambrecht, *Phys. Rev. B* **2013**, *88*, 165203.
[29] C. E. Patrick, K. W. Jacobsen, K. S. Thygesen, *Phys. Rev. B* **2015**, *92*, 201205.
[30] Z. Chen, C. Yu, K. Shum, J. J. Wang, W. Pfenninger, N. Vockic, J. Midgley, J. T. Kenney, *J. Lumin.* **2012**, *132*, 345.